

Revised Manuscript

Oxidation of Organic Functionalities by $\text{PhI}(\text{OAc})_2$ Catalysed by Magnetically Separable $\text{Fe}_3\text{O}_4@$ dopa-Supported Mn(III) Complexes: Combined Experimental and Theoretical Approach

Aratrika Chakraborty,^[a] Sanchari Dasgupta,^[a] Sourav Chatterjee^[b], Prof. Maria Isabel Menéndez,^[c] Prof. Debasis Das,^[a] Dr. Tanmay Chattopadhyay*^[b]

^[a]Department of Chemistry, University of Calcutta, 92 A. P. C. Road, Kolkata-700 009, India. E-mail: dasdebasis2001@yahoo.com

^[b]Department of Chemistry, Panchakot Mahavidyalaya, Sarbari, Purulia, 723121, India. E-mail: tanmayc2003@gmail.com.

^[c]Departamento de Química Física y Analítica. C/Julián Clavería, 8. 33006. Oviedo. Spain. E-mail: isabel@uniovi.es

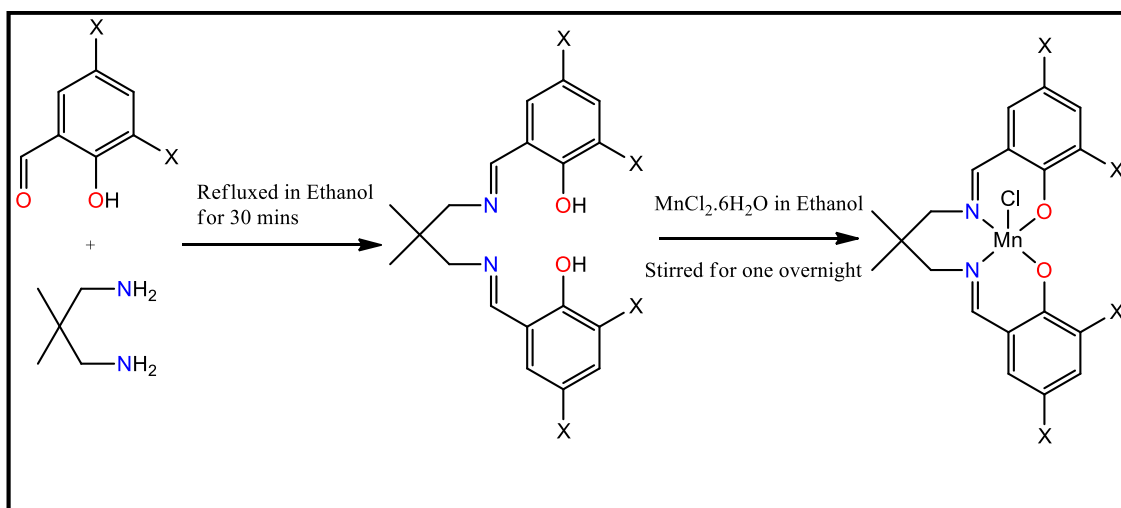
Abstract

Three newly designed ligands N, N'-bis (3, 5-diX)-2, 2-dimethylpropane-1, 3 diamine, where X=Cl/Br/I ($\text{H}_2\text{L}^1\text{-H}_2\text{L}^3$) having N_2O_2 binding sites, have been chosen to synthesize mononuclear manganese(III) complexes **1-3** with an aim to study their catalytic activity towards oxidation of various substrates using $\text{PhI}(\text{OAc})_2$ as a terminal oxidant. All these complexes have been characterized by routine physico-chemical techniques. Complexes **1** (MnL^1Cl) and **2** (MnL^2Cl) have further been structurally characterized by X-ray single crystal structure analysis. Detailed analysis of ESI-MS, UV-Vis and cyclic voltammetry studies along with theoretical calculations helped us to put forward probable mechanistic pathway for these efficient catalytic reactions. Complex **1** exhibited the highest catalytic efficiency in every reaction and therefore it was selected for building a magnetically separable catalyst by attaching it to surface modified magnetic nanoparticles. The new $\text{Fe}_3\text{O}_4@$ dopa@ MnL^1Cl (dopa=dopamine hydrochloride) [**FDM-1**] catalyst was characterized by solid state UV-VIS, FT-IR, SEM, TEM, TGA, PXRD, EDX and SQUID analyses. The catalytic activity towards oxidation of various substrates by **FDM-1** was studied using $\text{PhI}(\text{OAc})_2$ and results indicated excellent efficiency along with reusability.

Introduction

The oxidation of organic functionalities is an essential and extensively used organic reaction.^[1, 2, 3] The traditional metal-catalyzed oxidations present serious disadvantages, which raise the demand for eco-friendly processes and encourage the development of clean and practical oxidation reactions.^[4-7] Earlier oxidizing agents were mainly limited to PhIO, NaOCl, H₂O₂, TBHP, KHSO₅ and oxaziridines.^[8] Hypervalent iodine compounds present highly interesting features associated with oxidation, together with relevant drawbacks.^[9-13] The inconveniences of these oxidizing agents point to iodine (III) oxidants such as iodosobenzene, PhIO,^[14] and Iodosobenzene diacetate, [PhI(OAc)₂] in particular,^[13,15] as more practical ones. PhIO is a famed single oxygen atom donor in catalytic oxygenation reactions and in mechanistic studies of oxygen transfer reactions.^[5-8, 16] However, its low solubility in most organic media and its innate trend to disproportionation to PhI and iodoxybenzene (PhIO₂) on heating or extended storage at room temperature^[17] make it an inappropriate candidate for oxidation purposes. PhI(OAc)₂, a precursor in the formation of PhIO,^[18] comes as a panacea to all these problems owing to its solubility in most organic solvents, convenience in handling, and commercial availability, making it a popular choice as a starting material in the preparation of various hypervalent iodine(III/V) derivatives and as a demure and selective oxidant in non-catalytic organic reactions.^[13,17,19] To the best of our knowledge, despite such appealing qualities of PhI(OAc)₂, only few oxidation reactions, such as that of alcohols to carbonyl products,^[20] make use of it. Earlier reports^[13] showed that an efficient and convenient polymer-supported PhI(OAc)₂ reagent was planned for the oxidation of alcohols catalyzed by KBr in aqueous media, but primary alcohols were further oxidized to carboxylic acids. Additional reports concerning PhI(OAc)₂ come from Collman and Nam^[21, 22] and Xia and coworkers.^[23] Adam et al described the role of PhI(OAc)₂ in selective oxidation of alcohols catalyzed by chromium(III) salen complex.^[20] To add to the above reports, Nishiyama and co-workers^[24] showed that PhI(OAc)₂ is a better oxidant than PhIO in ruthenium-pyridine-2,6-dicarboxylate complex-catalyzed epoxidation of *trans*-stilbene.^[25] On the other hand, owing to their high activity, selectivity and enantioselectivity, metal salen complexes are extensively used in homogeneous catalysis.^[26-31] Easy availability of active sites of these homogeneous catalysts enhances their efficiency, but their separation from the reaction mixture is a challenging issue. Heterogeneous catalysts are a solution to this problem owing to their easy separation from the reaction mixture. However, these catalysts usually show lower catalytic activity due to the absence of accessible active sites. With all this in mind, a catalytic system which bears the advantageous features of both homo- and

heterogeneous catalysts would be highly desired. Magnetically separable nanocatalysts (MSNs) can be considered a bridge between homogeneous and heterogeneous catalysts. Magnetic stimulation provides unique characteristics such as eco-friendly nature, ease of recyclability and simple operation of the catalyst. ^[32-39] In addition, MSNs provides excellent surface-to-volume ratio which significantly amplifies the proximity between reactants and catalyst. This in turn, increases the overall activity of the catalyst for desired transformations. In the present work the synthesis of three Mn(III) Schiff base complexes is described. Their usefulness as homogeneous catalysts in the oxidation of different organic functionalities such as alcohols, alkanes, alkenes, aldehydes, amines, and sulfides, with $\text{PhI}(\text{OAc})_2$ as the oxidizing agent, is investigated. Experimental measurements along with theoretical calculations provide interesting hints about the molecular mechanism of the oxidation process and on the reasons that explain the oxidation capability of each metal complex. Complex **1**, with structural formula $[\text{MnL}^1\text{Cl}\cdot\text{CH}_3\text{CN}]$, becomes the most efficient catalyst followed by complexes **2** and **3** (see **Scheme 1**), steric factor seems to be playing a major role in determining the catalytic efficiency. The most effective catalyst is linked to magnetically separable nano-particles and its oxidative capability tested. The main goal of this work is the description of an economic, efficient and eco-friendly procedure for the oxidation of different organic functionalities that may be useful both in organic synthetic labs and even at the industrial scale.



Scheme 1 Synthetic route for the preparation of Mn complexes **1** ($\text{X} = \text{Cl}$), **2** ($\text{X} = \text{Br}$), and **3** ($\text{X} = \text{I}$).

Results and discussion

Preparation and characterization of homogenous catalysts

The synthesis of three purposely selected Schiff base ligands H_2L^1 , H_2L^2 and H_2L^3 was carried out by adding 3, 5-dichlorosalicylaldehyde, 3, 5-dibromosalicylaldehyde and 3, 5-diiodosalicylaldehyde separately to 2, 2-dimethyl-1,3-diaminopropane in ethanolic medium. [where $H_2L^1 = N, N'$ -bis (3, 5-dichlorosalicylidene)-2, 2-dimethylpropane-1, 3 diamine, $H_2L^2 = N, N'$ -bis (3, 5-dibromosalicylidene)-2, 2-dimethylpropane-1, 3-diamine, $H_2L^3 = N, N'$ -bis (3, 5-diiodosalicylidene)-2, 2-dimethylpropane-1, 3 diamine]. Further treatment of H_2L^1 , H_2L^2 and H_2L^3 with manganese (II) chloride hexahydrate gave complexes **1**, **2** and **3**, respectively (see Scheme 1), where in every case Mn(II) undergoes aerial oxidation to Mn(III). X-ray diffractable single crystals of **1** and **2** were obtained from DMF solvent. The complexes were characterized by usual physiochemical methods. FTIR spectral studies reveal that all of them exhibit bands in the range of 1614-1623 cm^{-1} due to the C=N stretching and skeletal vibration in the range of 1545-1580 cm^{-1} (Figures S1-S3). Electronic absorption spectra of the complexes in acetonitrile medium show intense bands in the UV and visible regions (Figure S4). The absorption maxima observed in the near-UV regions (below 300 nm) for these complexes are caused by $\pi-\pi^*$ transitions involving the phenolate units. The lower energy bands (around 380 nm) are proposed to arise due to charge-transfer transitions from the in-plane $p\pi$ orbital of the phenolate to the half-filled $d\pi^*$ orbital of Manganese(III).^[40,41] Electrospray Ionisation Mass Spectrometry (ESI-MASS) studies of all the three complexes have been performed (Figures S5-S7). Molar conductance of complexes **1-3** in acetonitrile medium are 2.2, 4.6, 5.7 $\Omega^{-1}cm^2M^{-1}$, respectively, which implies that all are non-electrolyte in solution.

Description of crystal structures of $[MnL^1Cl.(CH_3CN)]$ and $[MnL^2Cl(CH_3CH_2OH)]$

The X-ray structure of complex **1** indicates that it crystallizes in orthorhombic space group $Pna21$ where the metal centre adopts a roughly distorted square-pyramidal geometry ($\tau = 0.08$, $\tau = 1$ for a regular trigonal bipyramid and $\tau = 0$ for a perfectly square pyramidal geometry)^[42] having two phenolic O atoms and the two imine N atoms on the basal plane with a chloride ion in the axial position with an acetonitrile as uncoordinated moiety (Figure 1 (A), Table S1) The N_2O_2 ligand donors occupy the equatorial plane with the Mn1–O1 and Mn1–O2 (phenolic O) distances of 1.861 Å and 1.899 Å respectively, and the Mn1–N1 and Mn1–N2 distances of 2.035 Å and 2.020 Å, respectively. Interestingly, the complex **1** adopts

an umbrella shaped structure, perhaps, to avoid the steric as well as electronic repulsion between the neighbouring chlorine atoms. The lattice diagram of complex **1** in Figure 1(B) shows that two molecular units are connected to each other via two weak hydrogen bonds to form a dimer where a chlorine atom of para position of an aromatic ring act as H-bond acceptor and the hydrogen of the $-\text{CH}_2-$ beside the imine act as H-bond donor vice versa (Table S5). These dimeric units are connected to each other via several weak interactions such as $\text{CH}\cdots\pi$ interactions between the aromatic ring of one unit and $-\text{CH}_2-$ of another, $\text{CH}\cdots\text{O}$ type interactions between the hydrogen of acetonitrile unit and oxygen of phenolic $-\text{OH}$ of the aromatic ring and $\text{CH}\cdots\text{Cl}$ interactions between the co-ordinated chlorine atom of one unit and aromatic hydrogen of another unit (Figures 1E and 1C, Tables S3 and S4). These layers are further connected by another type of weak $\text{CH}\cdots\text{Cl}$ interaction (Figure 1D, Table S5).

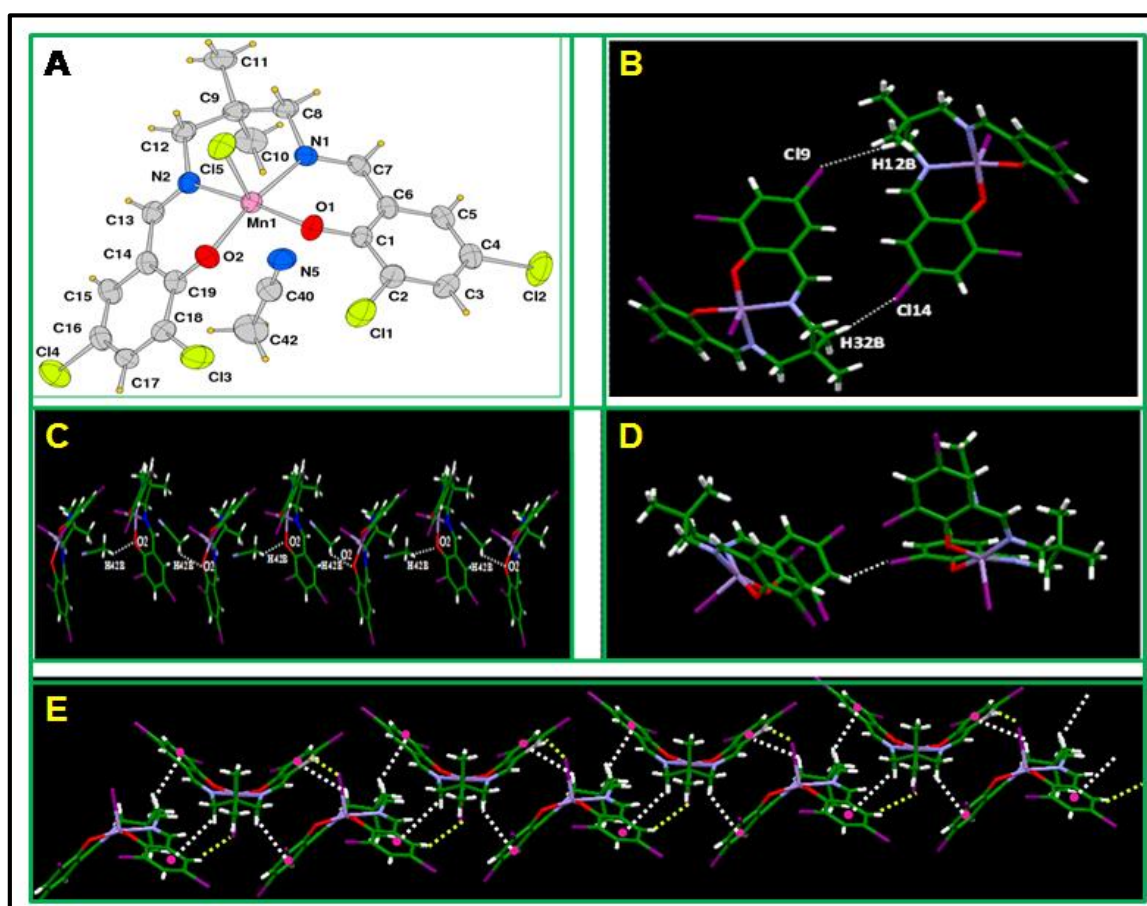


Figure 1. (A) ORTEP drawing (50% probability ellipsoid) of complex **1** (B) Different types of $\text{C}-\text{H}\cdots\text{Cl}$ interactions. (C) Different types of $\text{CH}\cdots\text{O}$ interactions. (D) Different types of $\text{CH}\cdots\pi$ (white colored line) and $\text{CH}\cdots\text{Cl}$ (yellow colored line) interactions. (E) Different types of $\text{CH}\cdots\pi$ (white colored line) and $\text{CH}\cdots\text{Cl}$ (yellow colored line) interactions.

Complex **2** crystallizes in the monoclinic space group P21/c where the metal centre is hexa-coordinated. Like complex **1** two phenolic O atoms and the two imine N atoms form the basal plane where as a chloride ion and an ethanol molecule are in the axial position in the complex **2** complex as shown in Figure 2A (Table S2). The N₂O₂ ligand donors occupy the equatorial plane with the Mn–O1 and Mn–O2 (phenolic O) distances of 1.878 Å and 1.915 Å, respectively, and the Mn–N1 and Mn–N2 distances of 2.031Å and 2.031Å, respectively. Complex **2** also adopts an umbrella shaped conformation due to the reason mentioned in case of complex **1**. The lattice diagram of complex **2** shows the molecular units are connected by several weak interactions like complex **1** but in lesser extent. The difference in electronegativity between chlorine and bromine may be the reason. The neighbouring molecular units are connected by mainly three type of weak interactions : i) CH··O interaction between the phenolic oxygen of one unit and aromatic hydrogen of another unit, ii) CH··π interaction between the aromatic ring of one unit with the hydrogen of the methyl group of another unit, iii) a weak H-bonding interactions between the hydrogen of ethanol and the coordinated chlorine atom to form a one dimensional layer [Figure 2B, Table S5 and S6]. These layers are connected via weak CH··Br interactions [Figure 2C, Table S5].

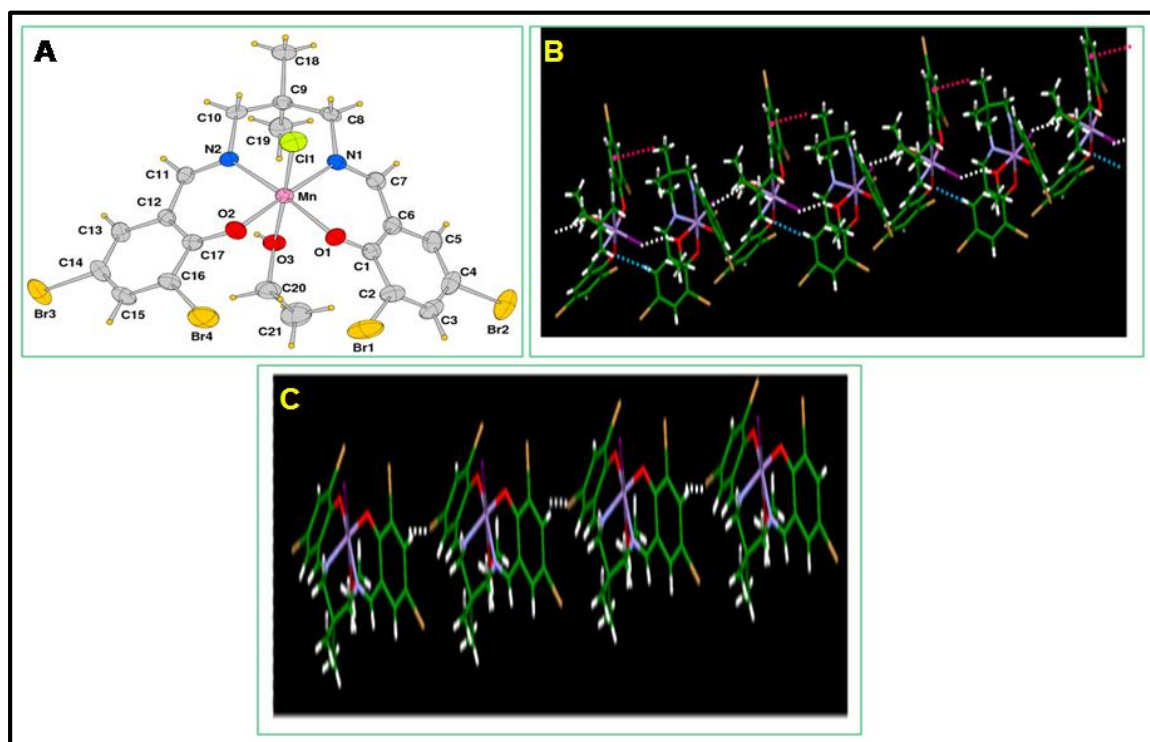


Figure 2. (A) ORTEP drawing (50% probability ellipsoid) of complex **2** (B) Different types of CH $\cdots\pi$ (red colored line), H \cdots Br (white colored line) interactions and CH \cdots O interactions (skyblue colored line). (C) Different types of CH \cdots Br interactions.

Tuning of homogeneous catalytic conditions

In all of the oxidation reactions, the amount of catalyst, the oxidant concentration and the time required to obtain the maximum yield were optimized. Table **1** collect isolated yield (%), conversion (%) and TON for the six types of oxidations tested. Notably, the effect of halogen substituents at ligand's backbone will become apparent in these experiments.

Alcohol Oxidation

To optimize the experimental conditions for alcohol oxidation to aldehyde, benzyl alcohol was initially chosen as the model substrate. Concentration of the catalyst varied between 0.01 and 0.5 mmol per 1 mmol of substrate. Yield increased when the amount of catalyst rose from 0.01 mmol to 0.1 mmol but remained stable with further increment of catalyst. Amounts of PhI(OAc)₂ between 1 and 2 mmol per 1 mmol of substrate were considered. Reaction time varied between 2 and 6 h. We observed that the aldehyde yield attained the peak after 4 h of reaction and remained the same even after 6 h. An optimum 0.01 mmol of catalyst, 1.25 mmol of PhI(OAc)₂ and 4 h reaction time are ideal for achieving the best yield. In order to explore the general applicability of our homogeneous catalysts **1-3**, various aliphatic and aromatic alcohols were subjected to oxidation under these optimized conditions in CH₃CN. Over oxidation of aldehydes to carboxylic acids were controlled. From Table **1** (Entries **1-5**) it can be observed that benzyl alcohol transforms to benzaldehyde with 85% conversion without formation of benzoic acid as side products in case of complex **1**. Aliphatic Alcohols (entries **2, 3**) shows good conversion as well as yield to the corresponding aldehydes. All the alcohols under study were oxidized smoothly to give aldehydes with complete selectivity. As is evident from Table **1** (entries **1-5**) catalyst **1** emerges as the best catalyst amongst the three.

Alkane Oxidation

Catalytic oxidation of hydrocarbons is a challenging task in organic chemistry since activation of the benzylic C-H bonds of alkanes is tough due to their strength. The required activation energy to overpower their stability leads to deeper oxidation products compared to selective products.^[3c] For this purpose the catalytic efficiency of homogeneous catalysts Complexes **1-3** was examined. In this case, the oxidation of ethylbenzene to acetophenone was initially chosen to find the optimal reaction conditions. Concentration of the catalysts

was varied between 0.01 and 0.1 mmol per 1 mmol of the substrate, the amount of $\text{PhI}(\text{OAc})_2$ changed between 0.5 and 2 mmol, and the time period ranged between 2 and 5 h. The best ketone yield for 1 mmol of ethylbenzene was obtained for 0.01 mmol of catalyst and 1.5 mmol $\text{PhI}(\text{OAc})_2$ during 5 h reaction time. **Table 1 (entries 6-8)** displays the experimental results. From Table 1 (entries 6-8) it can be observed that ethylbenzene transforms to acetophenone with 88% conversion and 92% yield with no such by products in case of complex 1. Diphenylmethane converts to Benzophenone as the only product with 89% conversion and 94% yield in case of complex 1, 86% conversion and 92% yield in case of complex 2 and 84% conversion and 91% yield in case of complex 3. Tetraline converts to α -tetralone as the only product with 87% conversion and 90% yield in case of complex 1. The isolated yield of the corresponding ketone in CH_3CN ranges from 83% - 94%. Again Catalyst **1** shows highest yields in comparison with catalysts **2** and **3**.

Alkene Epoxidation

We selected the epoxidation of (E)-stilbene as the model reaction in this section. The catalyst concentration was varied between 0.01 mmol and 0.1 mmol per 1 mmol of substrate, $\text{PhI}(\text{OAc})_2$ between 1 and 1.5 mmol per 1 mmol of substrate, and time between 2 and 6 h. An optimum concentration of 0.01 mmol catalyst, 1.4 mmol $\text{PhI}(\text{OAc})_2$, and 4 h reaction time were ideal for achieving the best yield of epoxide. With these optimized reaction conditions, we considered other alkene substrates. Our catalytic system showed high activity in epoxidation of (E)-Stilbene and (Z)-Stilbene rendering yields closer to 91% and 93% in case of complex 1 affording the corresponding epoxides as the only product. Epoxidation of Styrene yielded 96% of styrene oxide with no such by products after 4 h. The epoxidation of alkenes such as (Z)-stilbene and styrene catalyzed by our synthesized catalysts **1**, **2** and **3** showed good yields for the desired products. Our results are summarized in **Table 1 (entries 9-11)**. The isolated yield of the corresponding epoxide in CH_3CN ranges from 83% - 96%.

Aldehyde oxidation

We selected oxidation of benzaldehyde to benzoic acid as the model reaction to evaluate the optimal reaction conditions. Herein the amount of the catalyst was varied between 0.01 mmol and 0.05 mmol per 1 mmol of substrate. In this case no such increment in yield was observed when the amount of the catalyst increased to 0.1 mmol. Sluggish increment in yield was found when concentration of $\text{PhI}(\text{OAc})_2$ exceeded 1.4 mmol. An optimum amount of 0.01 mmol of catalyst, 1.2 mmol of $\text{PhI}(\text{OAc})_2$ and 3 h reaction time were found to be ideal for

achieving the best yield of carboxylic acid. Successful results prompted us to proceed further with other aldehydes whose results are summarized in **Table 1 (entries 12-15)**. As is evident from **Table 1** (entry 1) benzaldehyde transforms to benzoic acid with conversions ranging from 93-97% and yields ranging from 96-99 % in case of complexes 1-3. For para substituted benzaldehydes (entries 13-14) conversion to corresponding aldehydes are appreciable with conversion values ranging from 92-96% in case of entry 13 and 80-85% in case of entry 14. Here as well catalyst 1 emerged as the best catalyst as is evident from Table 1 (entries 12-15).

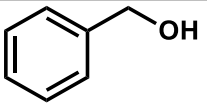
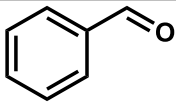


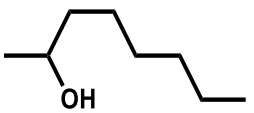
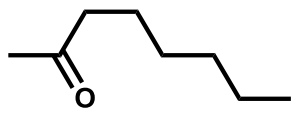
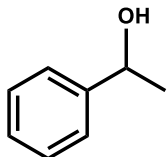
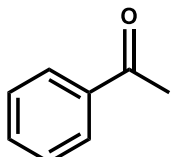
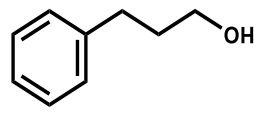
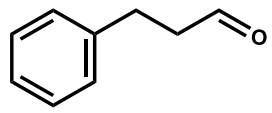
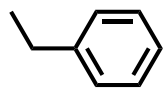
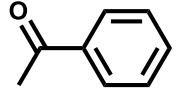
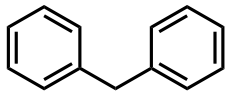
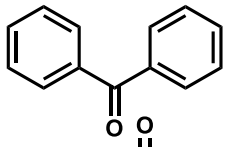
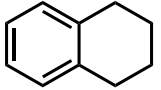
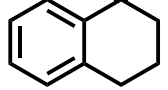
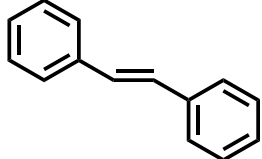
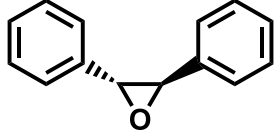
Amine oxidation

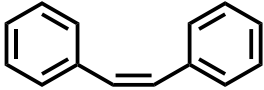
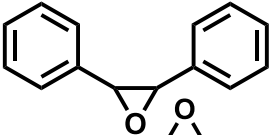
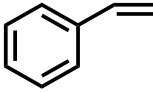
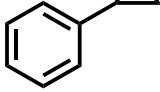
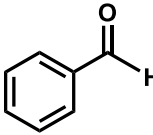
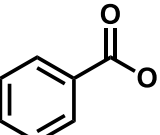
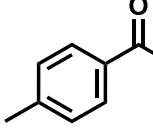
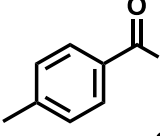
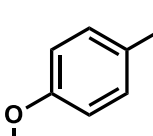
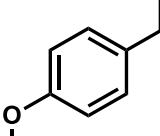
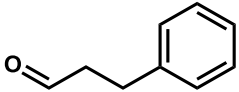
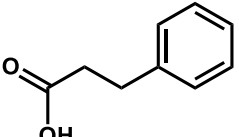
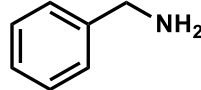
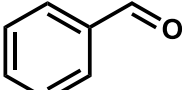
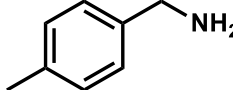
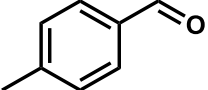
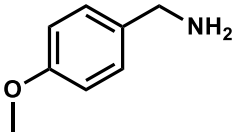
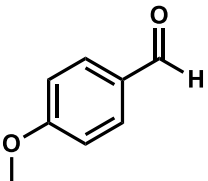
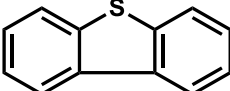
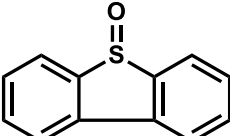
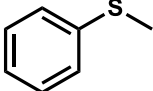
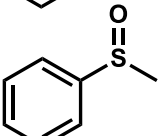
For studying the oxidation of amines, 4-methylbenzylamine was regarded as the model substrate to judge the optimal conditions. Increment of catalyst concentration beyond 0.1 mmol did not result in appreciable increase in yield, and a concentration of 0.01 mmol was judged to be the ideal one. Varying amounts of $\text{PhI}(\text{OAc})_2$ between 0.05 and 1.2 mmol per 1 mmol of substrate were employed and 1mmol was seen as the best choice. Time varied between 3-6 h, and 6 h were needed to reach the best yield. Our observations for this and other substituted benzylamines are summarized in **Table 1(entries 16-18)**. Benzyl amine transforms to benzaldehyde with conversion ranging from 84-90%. The isolated yield of the corresponding aldehydes from entries 16-18 in CH_3CN ranges from 81% - 93%.

Sulfide oxidation

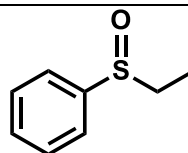
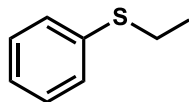
Here we took thioanisole as a test substrate. To optimize the amount the reaction conditions the amount of the catalyst was kept between 0.01 to 0.5 mmol per 1 mmol of substrate, concentration of $\text{PhI}(\text{OAc})_2$ oxidant was varied between 1-2 mmol, and time was varied between 3-6h. An optimum amount of 0.01 mmol of catalyst, 1mmol of $\text{PhI}(\text{OAc})_2$ and 6 h reaction time were found to be ideal for achieving the best yield of sulfone as the sole product. Considering the optimum conditions we proceeded to explore the substrate scope. Our results are summarized in **Table 1 (entries 19-21)**. All substrates were easily converted to sulfones with high yields and with selectivity greater than 99%. The isolated yield of the corresponding sulfones in CH_3CN ranges from 79% - 93%. Catalyst **1** shows higher yields in comparison with catalysts **2** and **3**.

Table 1 Summarized results of various substrate oxidation by $\text{PhI}(\text{OAc})_2$ catalyzed by complexes **1-3**

Entry	Substrate	Product	Conversion(%) ^a			Yield (%) ^b			TON ^c		
			1	2	3	1	2	3	1	2	3
Alcohol Aldehyde/ ketone											
1			85	83	76	95	90	87	80.75	74.7	66.12
2			87	86	80	97	92	85	84.39	79.12	68
3			85	82	80	80	75	70	68	61.5	56
4			95	92	88	99	95	90	94.05	87.4	79.2
5			92	88	80	99	90	85	91.08	79.2	68
Alkane Ketone											
6			88	85	81	92	90	87	80.96	76.5	70.47
7			89	86	84	94	92	91	83.66	79.12	76.44
8			87	82	80	90	87	83	78.3	71.34	66.4
Alkene Epoxide											
9			87	84	81	91	87	83	79.17	73.08	67.23

10			88	85	84	93	92	89	81.84	78.2	74.76
11			90	88	84	96	94	90	86.4	82.72	75.6
Aldehyde		Acid									
12			97	96	93	99	97	96	96.03	93.12	89.28
13			96	95	92	98	96	91	94.08	91.2	83.72
14			85	82	80	90	88	87	76.5	72.16	69.6
15			84	80	76	90	87	81	75.6	69.6	61.56
Amine		Aldehyde									
16			90	87	84	93	90	85	83.7	78.3	71.4
17			87	83	80	93	87	81	80.91	72.21	64.8
18			89	87	84	90	88	83	80.1	76.56	69.72
Sulfide		Sulfoxides									
19			89	86	83	88	82	79	78.32	70.52	65.57
20			90	87	82	93	89	80	83.7	77.43	65.60

21



88 84 82 90 87 81 79.2 73.08 66.42

Reaction conditions: Complex 1/2/3 (0.01 mmol), substrate (1 mmol) +

[1] For entries 1-5: $\text{PhI}(\text{OAc})_2$ (1.25 mmol), Alcohol (1 mmol), CH_3CN (10 m L). Stirring at 60°C for 4h.

[2] For entries 6-8: $\text{PhI}(\text{OAc})_2$ (1.5 mmol), alkane (1 mmol), CH_3CN (10 m L). Stirring at 60°C for 5h.

[3] For entries 9-11: $\text{PhI}(\text{OAc})_2$ (1.4 mmol), alkene (1 mmol) CH_3CN (10 m L). Stirring at room temperature for 4h.

[4] For entries 12-15: $\text{PhI}(\text{OAc})_2$ (1.4 mmol), aldehyde (1 mmol), CH_3CN (10 m L). Stirring at room temperature for 4h.

[5] For entries 16-18: $\text{PhI}(\text{OAc})_2$ (1 mmol), amine (1 mmol), CH_3CN (10 m L). Stirring at room temperature for 4h.

[6] For entries 19-21: $\text{PhI}(\text{OAc})_2$ (1 mmol), sulfide (1 mmol), CH_3CN (10 m L). Stirring at room temperature for 4h.

^[a]Determined by ^1H NMR analysis of the crude reaction mixture using tetramethylsilane, as internal standard.

^[b]Yields of the respective products are based on 100% conversion of the benzyl alcohol (entries 1-5), ethylbenzene (entries 6-8), (E)-Stilbene (entries 9-11), Benzoic acid (entries 12-15), benzyl amine (entries 16-18) and thioanisole (entries 19-21).

^[c] Turnover number (TON) = [(Total number of moles of product)/(moles of catalyst)].

Selectivity for all the systems were found to be >99%.

Mechanistic pathway

The interesting catalytic activity of all the synthesized complexes, especially complex **1** i.e $[\text{MnL}^1\text{Cl}(\text{CH}_3\text{CN})]$, prompted us to scrutinize some mechanistic aspects of the reaction and the nature of the active species involved. For this purpose UV-Vis spectroscopy and ESI-MS analysis were performed. The UV-Visible study shows initially a spectrum of complex **1** with bands at 385 nm which disappear immediately on addition of $\text{PhI}(\text{OAc})_2$, as shown in Fig. 3. On passage of time, peak at 333 nm and a shoulder at 435 nm gradually develop, which can be assigned to the generation of $\text{Mn}(\text{V})=\text{O}$ complex. These observations are well

synchronized with those observed when complex **1** was made to react with PhIO whereby two bands at 338 nm and 446 nm were generated due to the formation of Mn(V)=O species (Figure S8).

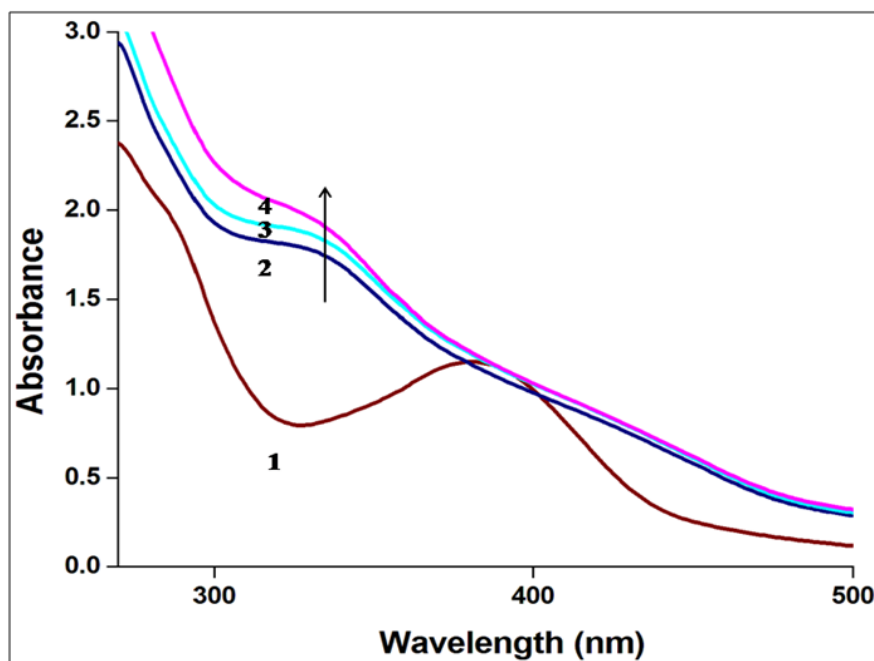


Figure 3. UV-Vis absorption spectra recorded: (1) complex **1**; (2-4) addition of PhI(OAc)₂ into complex **1** recorded after every 10 minutes [concentrations: complex **1** (5×10^{-4} M), 3mL; PhI(OAc)₂ 7.5×10^{-4} M, 3mL;]

In order to confirm our observations we performed an ESI-MS analysis. ESI-MS spectrometry is a convincing tool to characterize reaction intermediates.^[43-45] ESI-MS analysis of the reaction between **1** and PhI(OAc)₂ as well as PhIO were performed. Initially an aliquot of 5 μ L from a 1.5 mM stock solution of complex **1** in CH₃CN was analyzed by ESI-MS separately. As shown in Figure S5 a peak at m/z 500.9288 corresponds to complex **1** [(C₁₉H₁₆Cl₄MnN₂O₂)⁺, MW 501.09]. To characterize the intermediate species generated, a 1.5 mM solution of the complex **1** was made to react with 1.1 eq of PhI(OAc)₂, i. e., 5.5 μ L of PhI(OAc)₂ from its stock solution of 1.5 mM, for 15 mins at room temperature. Then 5 μ L of this solution was taken and analyzed by ESI-MS. The following ion peaks were observed: m/z 822.9014, m/z 666.9308, and m/z 516.9275, which correspond to [(Mn^{III}L¹)(PhI(OAc)₂)⁺], [(Mn^{IV}L¹)(OAc)]⁺ + 2CH₃CN + Na⁺ and [Mn^VL¹O]⁺, respectively (see **Figure 4**). Assembling our observations from ESI-MS and UV-Vis studies a probable mechanistic pathway can be sketched out. It is evident from the above described studies that

on addition of $\text{PhI}(\text{OAc})_2$ to complex **1** (**A** at **Scheme 2**) initial linking between these two species takes place followed by subsequent reorganization to adduct **B**, which could be duly arrested in ESI-MS and identified as $[(\text{Mn}^{\text{III}}\text{L}^1)(\text{PhI}(\text{OAc})_2)]^+$. Further expulsion of $\text{PhI}(\text{OAc})\cdot$ Radical ^[46] leads to the formation of species **C**, which was arrested in ESI-MS studies and identified as $[(\text{Mn}^{\text{IV}}\text{L}^1)(\text{OAc})]^+ + 2\text{CH}_3\text{CN} + \text{Na}^+$. Electron transfer between species **C** and $\text{PhI}(\text{OAc})\cdot$ radical ^[46] leads to the formation of $\text{Mn}(\text{V})=\text{O}$ species **D**.

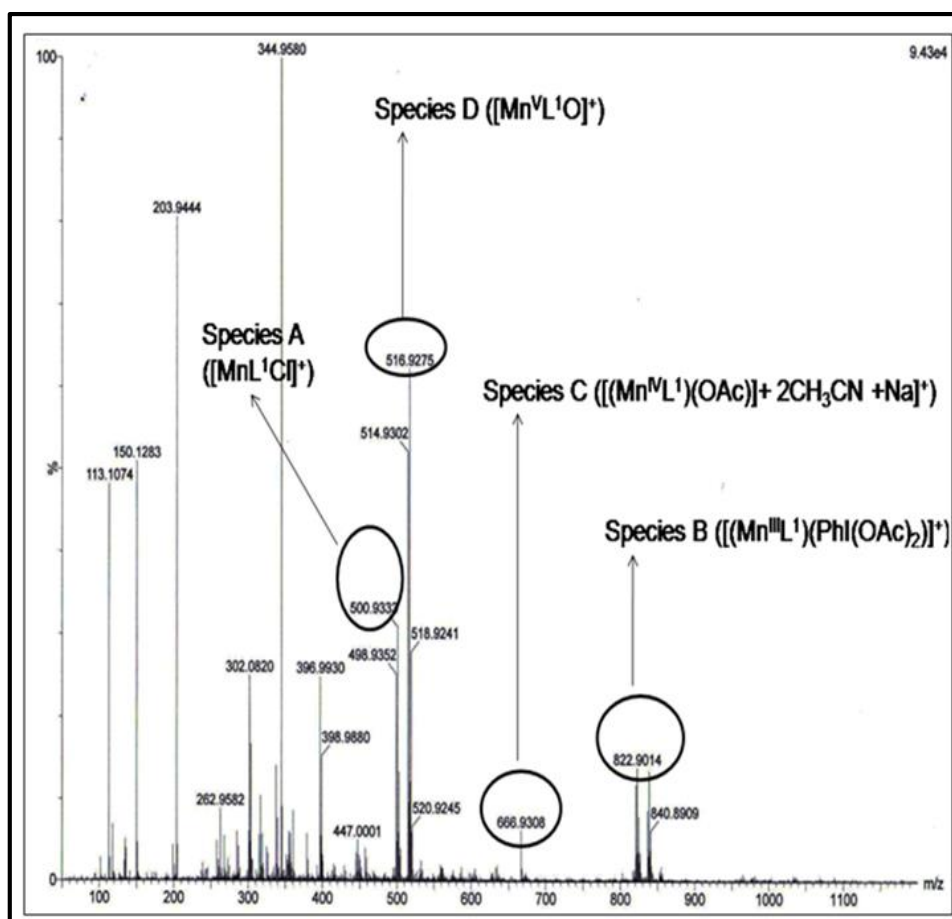
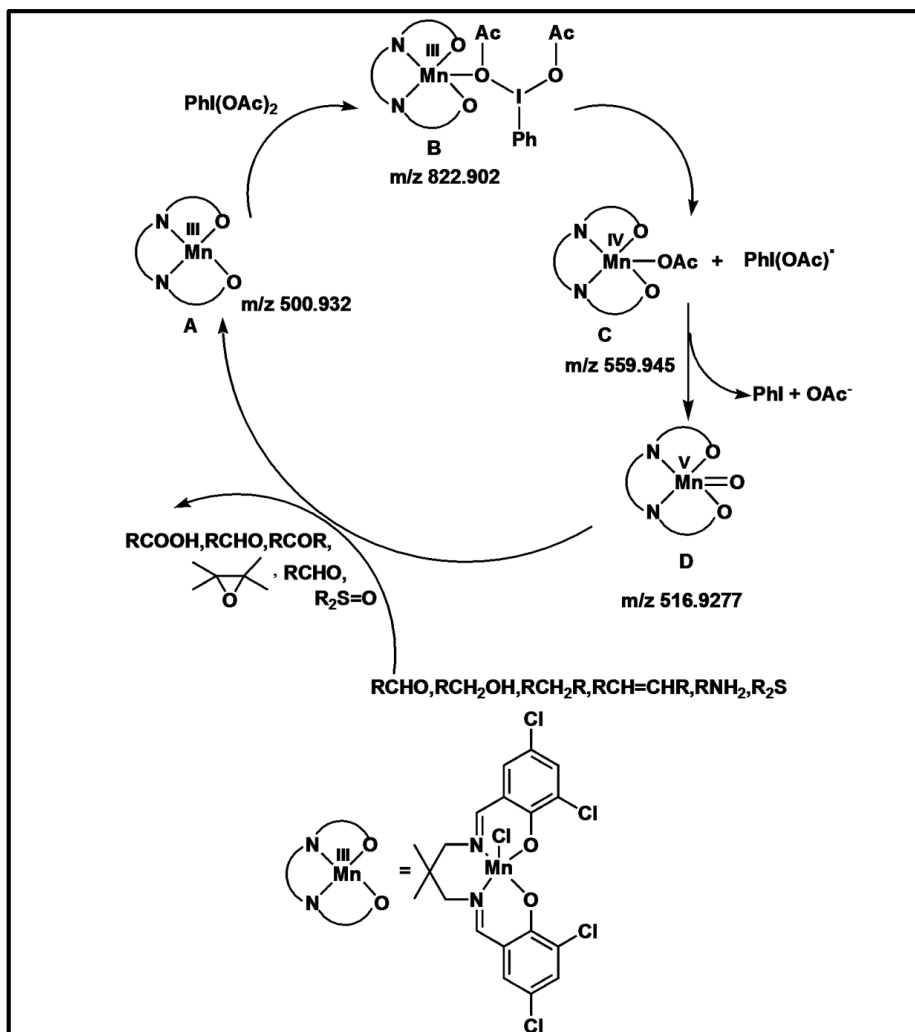


Figure 4. ESI-MASS spectrum of mixture of complex 1 and $\text{PhI}(\text{OAc})_2$.



Scheme 2. Mechanism for the Mn(III) Schiff base complex catalyzed oxidation and epoxidation by Iodosobenzene diacetate.

Electrochemical studies

We further studied electrochemistry of complex, **1**, in absence and presence of $\text{PhI}(\text{OAc})_2$ to confirm the formation of high-valence Mn(V)-oxo species. Cyclic voltammogram of the mononuclear Mn^{III} complex, **1**, has been recorded in acetonitrile medium over a potential range from -1.5 V to +1.5 V. It exhibits a quasi-reversible cyclic voltammetric response (Fig 5a). But after addition of $\text{PhI}(\text{OAc})_2$ cyclic voltammogram dramatically changed. The possible mechanism of this change according to observed potentials are discussed here. A single cathodic peak was observed at potential about -1.138 V (E_p^{c1}) when scanning toward cathodic direction whereas three anodic peaks at 0.629 V (E_p^{a1}), E_p^{a2} (1.225V) and E_p^{a3} (1.745 V) (Fig 5b) respectively, were observed when scanning toward anodic direction. The observed single cathodic peak in the negative scan generated due to reduction from Mn(V) to Mn(II). But a three stepwise oxidation from Mn(II) to Mn(III), then Mn(III) to Mn(IV) and

finally, Mn(IV) to Mn(V) were observed in the positive scan. These results unambiguously proved the generation of high-valence Mn(V)-oxo species.

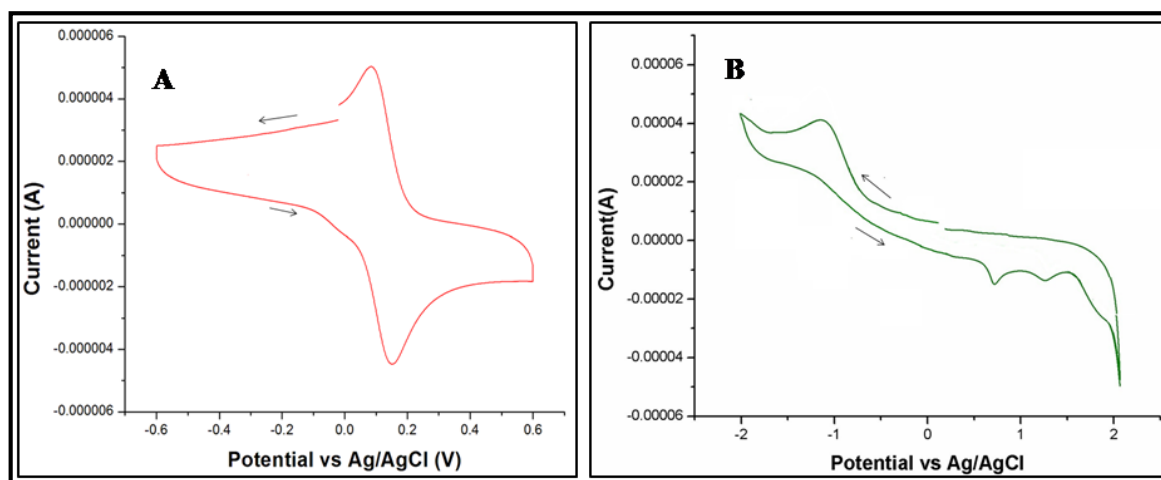


Figure. 5 (A) Cyclic Voltammogram of Complex 1 (1×10^{-3} M) in CH_3CN containing $(\text{Bu}_4\text{N})\text{ClO}_4$ as supporting electrolyte at a scan rate of 0.1 V s^{-1} . (B) Cyclic Voltammogram of Complex 1 and $\text{PhI}(\text{OAc})_2$ in CH_3CN containing $(\text{Bu}_4\text{N})\text{ClO}_4$ as supporting electrolyte at a scan rate of 0.1 V s^{-1} .

Theoretical investigation

Starting with a Mn(III) salen catalyst and a iodosylarene terminal oxidant, as in our case, several mechanistic pathways have been proposed in the literature for the oxidation of different substrates. The most commonly accepted one is the O-rebound mechanism that consists of the initial oxidation of the catalyst to $\text{Mn}(\text{V})=\text{O}$ species followed by the O-transfer to the substrate from this active form of the catalyst.^[47] However, it has also been suggested that, besides $\text{Mn}(\text{V})=\text{O}$, Mn salen complexes bonded to a iodosyl moiety, might act as active oxidation catalysts.^[48,49] In any case, the formation of type **B** adducts between each **1-3** Mn(III) complex and the oxidant, $\text{PhI}(\text{OAc})_2$, (see **Scheme 2**) is a significant step in the evolution towards any active catalyst and a stage where the nature of the substituents at the metal complex may exert large influence. To understand how the nature of the halogen substituents at the complexes affect the stability of the corresponding adducts, we have theoretically characterized all the isolated reactants (Mn(III) complexes and the oxidant) and all the adducts. The spin multiplicities available for the metal are 1, 3 and 5, and all of them have been tested in this work. The first one is discarded since it provides geometries for both the isolated and the adduct complexes that are very distorted and different from the experimental ones. Triplet and quintuplet structures show similar geometries, both close to the experimental ones, so we present and discuss here the results corresponding to both of

them. Figure 6 displays the general pattern for the reaction of the three initial Mn(III) complexes in their interaction with the oxidant to render the adducts.

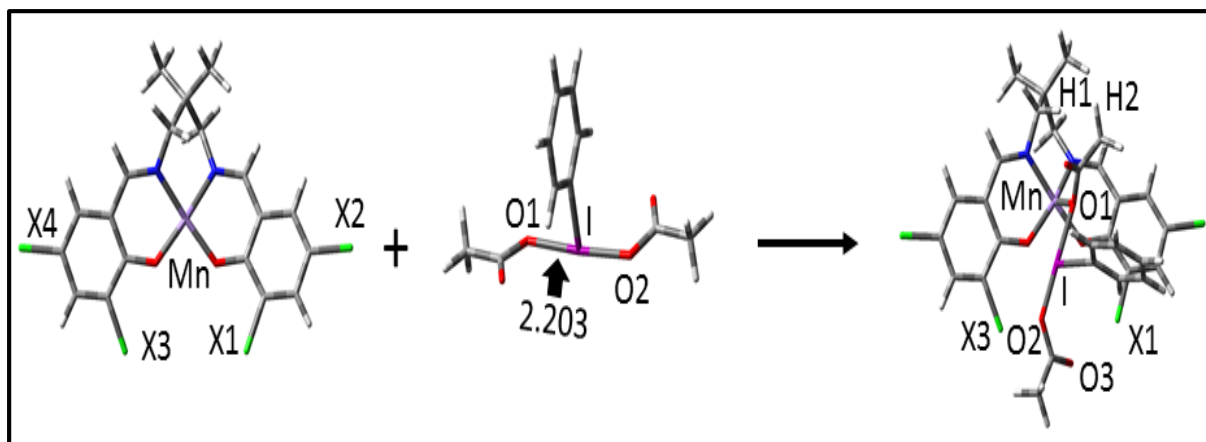


Figure 6. General scheme for the formation of adducts between Mn(III) complexes and $\text{PhI}(\text{OAc})_2$ oxidant. The distance between O1 and I in the isolated oxidant, in Å, is provided.

Table 2 shows the most relevant bond distances (in Å) for the three optimized adducts at the triplet and quintuplet spin state. **Table 3** collects the relative electronic and Gibbs energies of the adducts, that is, their stability with respect to the isolated reactants at both spin multiplicities.

Table 2. Most relevant bond distances (in Å) for the three B3LYP/6-31+G(d,p) optimized adducts at the triplet and quintuplet spin state.

Entry		X = Cl		X = Br		X = I	
		Triplet	Quintuplet	Triplet	Quintuplet	Triplet	Quintuplet
1	d(O1-Mn)	1.945	2.427	1.949	2.433	1.949	2.464
2	d(O1-I)	2.537	2.327	2.533	2.327	2.528	2.323
3	d(I-O2)	2.086	2.147	2.087	2.146	2.088	2.149
4	d(H1-H2)	2.548	2.408	2.570	2.425	2.624	2.544
5	d(X1-O3)	3.877	4.034	3.944	4.051	4.099	4.355

Table 3 Relative B3LYP/6-31+G(d,p)electronic and Gibbs energies in acetonitrile solution of the manganese complexes-oxidant adducts in both triplet and quintuplet spin states.

Adducts	ΔE (kcal/ml)		ΔG (kcal/ml)	
	Triplet	Quintuplet	Triplet	Quintuplet
X = Cl	-5.7	-0.5	9.6	15.6
X = Br	-4.9	-0.5	13.0	16.3
X = I	-2.9	-1.1	15.1	17.1

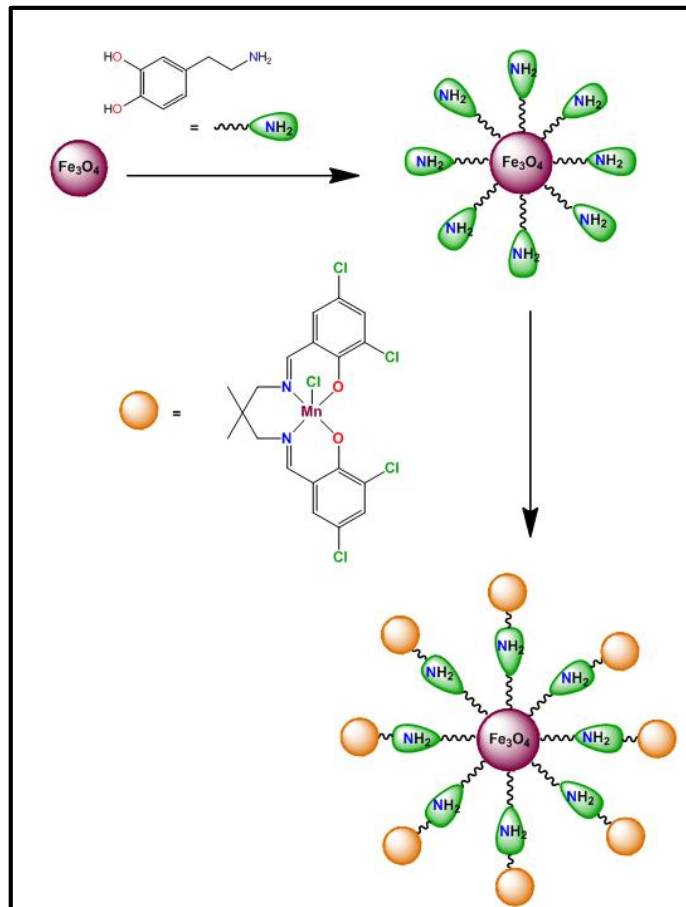
ΔG values at Table 4 show that, at both spin states, the stability of the complexes reduces as the size of the halogen substituents increases, in perfect agreement with experimental findings. Although structures with triplet spin state present higher absolute energy than those in quintuplet one (see **Table S7, S.I**), the most stable adducts form with the metal complexes in their triplet state. According to the numbering of this section, at both spin multiplicity states, the O1 atom of the oxidant bonds to manganese ion and gets away from the Iodine atom, that, consequently, gets closer to O2 (see entries 1, 2 and 3, **Table 2**). Two steric effects come into stage to explain the increasing stability of adducts as the size of the halogen reduces. On the one hand, the presence of a dimethyl substituted C atom at the bridge backbone of the Schiff ligand provokes a distortion of this area of the complex in such a way that the attacking acetate moiety is not allowed to come close to the metal due to steric repulsions (see entry 4, **Table 2**). On the other hand, the other end of the $\text{PhI}(\text{OAc})_2$ oxidant tries to fit into the room surrounded by X1 and X3 halogen atoms and here is where the size of the halogen plays its role. Chlorine is the smallest halogen here considered and the one that lets the closest and strongest approach of the oxidant to the manganese complex, thus rendering the most stable adduct. Following this line of reasoning it becomes clear that, as the size of the halogen increases, the oxidant is forced to establish a weaker interaction with the metal complex. We believe that the steric effects described for this initial reaction step may operate in the subsequent steps happening before the formation of $\text{Mn}(\text{V})=\text{O}$. Thus, if this initial step would not be the rate limiting one, its analysis clarifies the kind of interactions that explain the highest efficiency of chlorine catalysts in the reactions here considered.

Our group had previously found that Fe(III) halogen salen complexes (built from 1,2-diaminopropane) in conjunction with PhIO as terminal oxidant rendered the opposite efficiency for the oxidation of alkenes, that is, those catalysts with chlorine substituents were

the least effective and the efficiency raised with the increase in the halogen size.^[38, 39] However, apart from the change in the metal, the reactants here used show two decisive differences with respect to those in our previous work: the bridge in the salen ligand (coming from 2,2-dimethyl-1,3-propanediamine) and the oxidizing agent. Both are now much bulkier than in our previous work and both cooperate to yield the observed stabilities of the complex-oxidant adducts, as above explained.

Preparation and characterization of Fe₃O₄@dopa@MnL¹Cl

The preparation of magnetically separable nanoparticles is displayed in **scheme 3**. Synthesis and characterization of magnetic nanoparticles Fe₃O₄ and Fe₃O₄@dopa has been executed following earlier reported methods.^[38, 39] Preparation of Fe₃O₄@dopa@MnL¹Cl has been carried out by adding 1g of complex **1**, i.e., MnL¹Cl a dispersed acetonitrile solution of amine-functionalized nano-Fe₃O₄ (Fe₃O₄@dopa, 500 mg) followed by stirring of the mixture for 14 h at room temperature. The product was allowed to settle and then washed several times with acetonitrile, and dried under vacuum at 50 °C for 3h. In this study we only report the characterization of Fe₃O₄@dopa@MnL¹Cl (**FDM-1**), since complex **1** proved to be the most efficient catalyst in homogeneous solution.



Scheme 3 Schematic representation of the preparation of **Fe₃O₄@dopa@MnL¹Cl** particles.

Figure S9 shows the FTIR spectra of **FDM-1**. The peaks at around 580 cm⁻¹ and 631 cm⁻¹ are the innate absorptions of the Fe-O bond, which confirms the presence of iron oxide, as previously reported.^[38, 39] Dopamine incorporation is substantiated by the presence of a peak around 1486 cm⁻¹ which can be attributed to the vibration of the benzene ring present at dopamine moiety. Several new peaks are generated for Fe₃O₄@dopa@MnL¹Cl, along with the characteristic peak of Fe₃O₄. The peak at 1527 cm⁻¹ may be assigned to the skeleton vibration of the complex; the salient peak at 1648cm⁻¹ may be due to the C=N vibration of the incorporated complex moiety. Hence the FTIR spectrum aids to conclude that the desired surface modification of MNPs has been efficaciously done. The degree of crystallinity of magnetic Fe₃O₄, Fe₃O₄@dopa described by PXRD has already been reported in our previous work.^[38,39] The PXRD pattern of our magnetically separable nanocatalyst Fe₃O₄@dopa@MnL¹Cl (Figure S10) clearly shows that Fe₃O₄ and Fe₃O₄@dopa have been incorporated, as proved by the presence of diffraction peaks at 2θ= 29.69°, 35.19°, 42.61°, 56.5°, 59.5° and 62.36°, which can be assigned to the (220), (311), (400), (422), (511) and (440) planes of Fe₃O₄, as earlier reported.^[38, 39] Solid state UV spectrum of Fe₃O₄@dopa@MnL¹Cl is shown in Figure S11. The existence of Fe₃O₄ in the Fe₃O₄@dopa and Fe₃O₄@dopa@MnL¹Cl species has been proved by comparison of the corresponding solid state UV-Vis spectra. MnL¹Cl has a broad shoulder at 460 nm (Figure S11). Increment of the absorbance around 490 nm for Fe₃O₄@dopa@MnL¹Cl clearly suggests the conjugation of MnL¹Cl onto Fe₃O₄@dopa. For further authentication of the successful surface modification of magnetic Fe₃O₄ and further inculcation of MnL¹Cl on the surface of Fe₃O₄@dopa, thermogravimetric analysis (TGA) was carried out (see Figure S12). TGA results clearly suggest that the enhancing weight loss is due to the increasing amount of attached organic moiety from Fe₃O₄@dopa to Fe₃O₄@dopa@MnL¹Cl. These results are in agreement with those earlier reported by our group.^[38, 39] Scanning electron microscopy (SEM) image of Fe₃O₄@dopa@MnL¹Cl in Fig. 7(a) depicts morphologies which are quite different from those of Fe₃O₄-NPs and Fe₃O₄@dopa previously reported.^[38, 39] Amendments in morphology are clearly visible when comparing those of Fe₃O₄ and Fe₃O₄@dopa. Transmission electron microscopy (TEM) images of Fe₃O₄@dopa@MnL¹Cl are depicted in Figure 7(b). A close look into these images reveals that the magnetic nanoparticles are rod like structures with average diameter lying within 50 nm. Energy-dispersive X-ray spectroscopy (EDX) spectrum of Fe₃O₄@dopa@MnL¹Cl is depicted in Figure 8(a). Signals

of Fe and O can be attributed to those coming from Fe_3O_4 nanoparticles and signal of C comes from Dopamine. Signals of Mn and Cl can be attributed to the complex moiety, thus successful confirming surface modification.

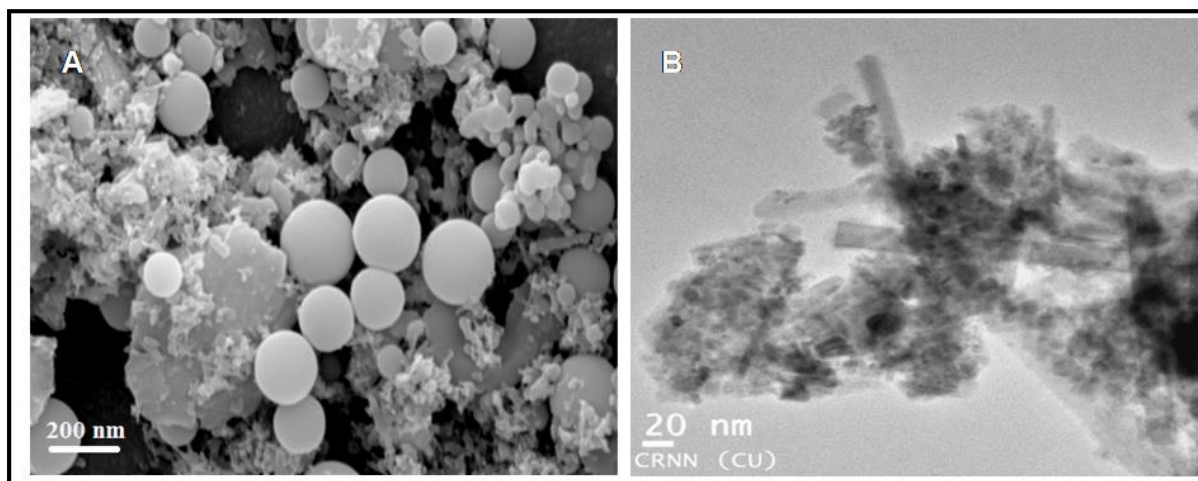


Figure 7. (A) SEM and (B) TEM images of $\text{Fe}_3\text{O}_4@\text{dopa}@\text{MnL}^1\text{Cl}$.

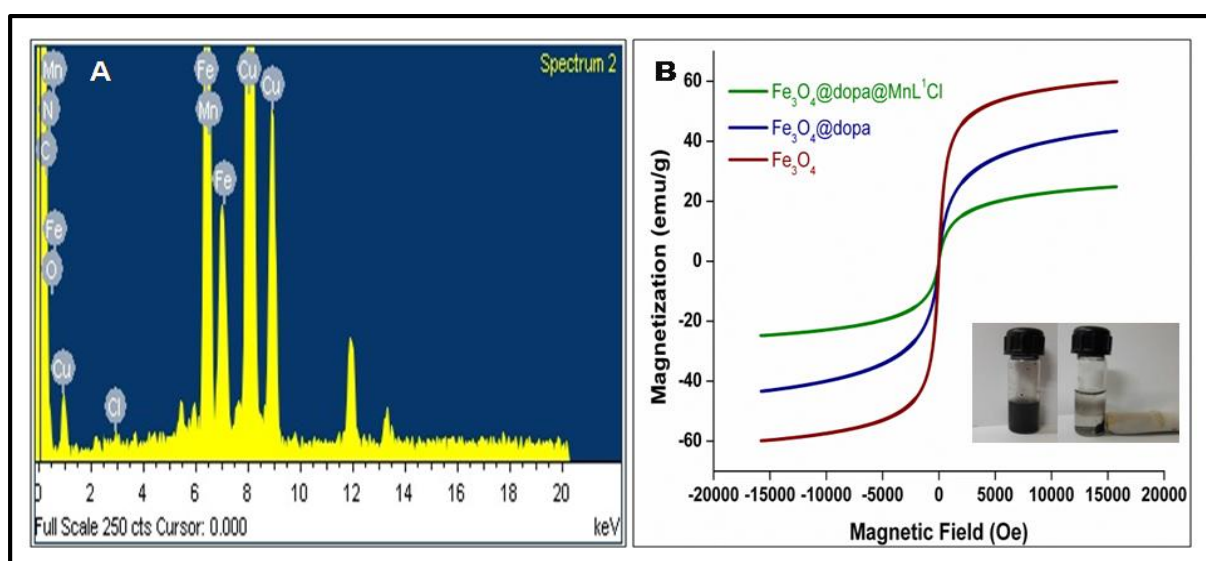


Figure 8. (A) Energy-dispersive X-ray (EDX) spectrum of $\text{Fe}_3\text{O}_4@\text{dopa}@\text{MnL}^1\text{Cl}$ (B) Magnetic curves of Fe_3O_4 NPs, $\text{Fe}_3\text{O}_4@\text{dopa}$ and $\text{Fe}_3\text{O}_4@\text{dopa}@\text{MnL}^1\text{Cl}$

Results of the magnetic behaviour of the Fe_3O_4 -NPs, $\text{Fe}_3\text{O}_4@\text{dopa}$, $\text{Fe}_3\text{O}_4@\text{dopa}@\text{MnL}^1\text{Cl}$ nanoparticles under the applied magnetic field are represented in Figure 8(b). There is a decrease in the values of the saturation magnetization (M_s) from the Fe_3O_4 nanoparticles (59.75 emu g^{-1}) to $\text{Fe}_3\text{O}_4@\text{dopa}$ (43.31 emu g^{-1}) and to the final **$\text{Fe}_3\text{O}_4@\text{dopa}@\text{MnL}^1\text{Cl}$** nanocatalyst (24.93 emu g^{-1}) which can be credited due to gradual increment of diamagnetic organic materials from Fe_3O_4 to $\text{Fe}_3\text{O}_4@\text{dopa}@\text{MnL}^1\text{Cl}$. In comparison with the bulk

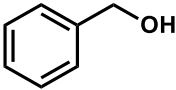
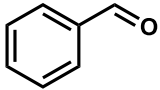
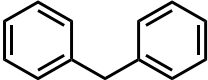
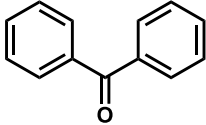
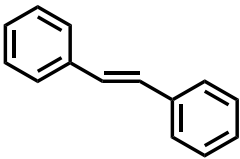
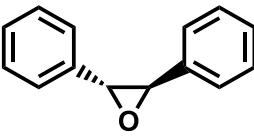
magnetite nanomaterials, that have a typical saturation magnetization value of 92 emu g^{-1} , the M_s value of the Fe_3O_4 nanoparticles is found to be much lower. Since the magnetization of a particle in an external field is a function of its size, it is expected that nanoparticles will generate a humble M_s value. ^[50] However, the net magnetism exhibited by the final nanocatalyst is enough to execute effective separation from the solution medium using an external magnetic force.

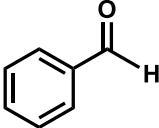
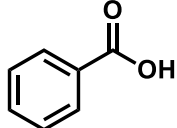
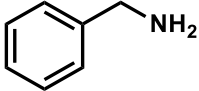
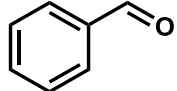
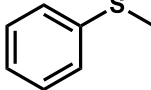
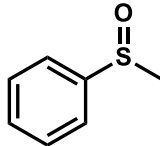
Oxidation properties of FDM-1

We have also searched the optimum reaction conditions for the oxidation of organic functionalities assisted by the heterogeneous catalyst, as already done for the homogeneous systems. For this purpose we initially examined catalyst loading whereby a variable weight of **FDM-1** between 100 and 250 mg was used per 1 mmol of benzyl alcohol. Enhancement in the yield of aldehyde was observed when the amount of catalyst was increased from 100 to 150 mg but the yield remained constant with further increase of catalyst amount. Varying amounts of terminal oxidant ($\text{PhI}(\text{OAc})_2$) and time were also considered. Optimum yield for alcohol oxidation was obtained by using 1.5 mmol of $\text{PhI}(\text{OAc})_2$ and 4h of stirring (entry 1 at Table 4). Similarly, for alkane oxidation we selected diphenylmethane as the test substrate. A variable weight of **FDM-1** between 50-200 mg was used per 1 mmol of diphenylmethane. No such advancement in yield was observed when the amount of catalyst was increased beyond 150 mg. The amount of $\text{PhI}(\text{OAc})_2$ was kept between 0.5-2 mmol and a concentration of 1.75 mmol was found to be an ideal one along with 6h stirring (entry 2 at Table 4). Critical amount of catalyst for alkene epoxidation reaction was similarly evaluated (entry 3 at Table 4). The weight of **FDM-1** was varied between 100-200 mg per 1 mmol of *E*-Stilbene. Concentration of $\text{PhI}(\text{OAc})_2$ was varied between 1-1.5 mmol. Results showed that using 1.25 mmol of $\text{PhI}(\text{OAc})_2$, 160 mg of **FDM-1** per 1 mmol of *E*-Stilbene and 5h stirring supplied the best yield. For aldehyde and amine oxidation (entries 4 and 5 at Table 4) concentration of **FDM-1** was varied between 75-200 mg. Oxidant loading was also examined. For both aldehyde and amine oxidation the yield remained unaffected by concentrations of $\text{PhI}(\text{OAc})_2$ beyond 1.5 mmol, so a concentration of 1.2 mmol was judged to be the ideal one. In case of sulfide oxidation (entry 6 at Table 4) catalyst concentration beyond 150 mg showed no effect in yield, so a concentration of 125 mg was selected to be the ideal one. $\text{PhI}(\text{OAc})_2$ concentration was varied between 1-1.5 mmol along with 6h stirring. At the end of each reaction, the catalyst was magnetically separated out and reused for further oxidation

reactions. Here it is noteworthy that we did not find any leaching of catalysts during the epoxidation reaction.

Table 4. Oxidation of various substrate by $\text{PhI}(\text{OAc})_2$ catalyzed by **FDM-1**

Entry	Substrate	Product	Catalyst, Reaction conditions	Conversion (%) ^a	Yield (%) ^{b,c}	TON ^d
1			FDM-1 (150 mg), substrate (1 mmol), $\text{PhI}(\text{OAc})_2$ (1.5 mmol), 4h, 60°C.	84	90(>99%)	75.6
2			FDM-1 (100 mg), substrate (1 mmol), $\text{PhI}(\text{OAc})_2$ (1.75 mmol), 6h, 60°C.	82	90(>99%)	73.8
3			FDM-1 (160 mg), substrate (1 mmol), $\text{PhI}(\text{OAc})_2$ (1.25 mmol), 5h, 60°C.	85	90(>99%)	76.5

4			FDM-1 (165 mg), substrate (1 mmol), PhI(OAc) ₂ (1.2 mmol), 4h, 60°C.	89	85(>99%)	75.65
5			FDM-1 (150 mg), substrate (1 mmol), PhI(OAc) ₂ (1.2 mmol), 3h, 60°C.	88	91(>99%)	80.08
6			FDM-1 (125 mg), substrate (1 mmol), PhI(OAc) ₂ (1.5mmol), 6h, 60°C.	80	88(>99%)	70.4

^[a] Determined by ¹H NMR analysis of the crude reaction mixture using TMS as internal standard.

^[b] Yields of the respective products are based on 100% conversion of the benzyl alcohol (entry 1), ethylbenzene (entry 2), (E)-Stilbene (entry 3), Benzoic acid (entry 4), benzyl amine (entry 5) and thioanisole (entry 6).

^[c] Values in parenthesis indicates selectivity.

^[d] Turnover number (TON) = [(Total number of moles of product)/(moles of catalyst)].

Reusability of Fe₃O₄@dopa@MnL¹Cl

The recyclability of our newly synthesized magnetically separable nanocatalysts has also been assessed. A series of experiments have been carried out by performing oxidation of benzyl alcohol, diphenylmethane, (*E*)-stilbene, benzaldehyde, benzylamine, and thioanisole catalyzed by $\text{Fe}_3\text{O}_4@\text{dopa}@\text{MnL}^1\text{Cl}$ nanocatalysts with the target of examining their activity after five runs. After each run the catalysts were recovered by application of a magnet. Then, these catalysts were washed with acetonitrile to remove any absorbed products and then dried. The used-up catalysts were further characterized by SEM (Figure S13), TEM and FTIR. (Figure 9) The results support the fact that the catalyst are stable with efficient activity in all the above described reaction runs.

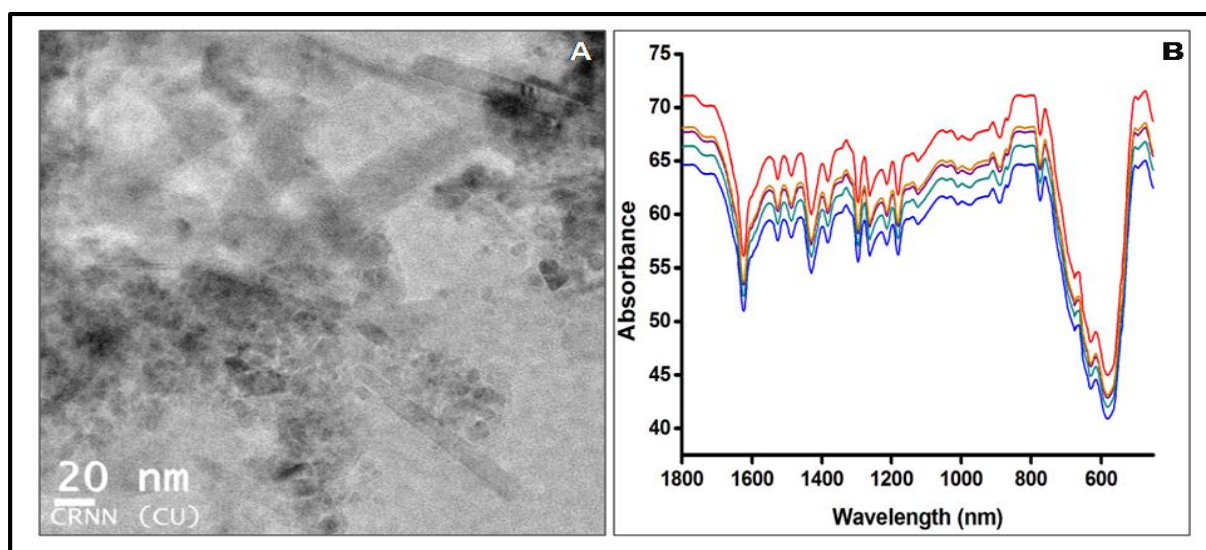


Figure 9. (A) TEM Image of reused $\text{Fe}_3\text{O}_4@\text{dopa}@\text{MnL}^1\text{Cl}$ (B) FTIR spectra of $\text{Fe}_3\text{O}_4@\text{dopa}@\text{MnL}^1\text{Cl}$ (five runs)

CONCLUSION

We have designed three coordination compounds of Mn(III) with three Schiff base ligands having N_2O_2 donor site, which were structurally characterized by single-crystal X-ray diffraction. These complexes were tested as homogeneous catalysts in the oxidation of alcohols, alkanes, aldehydes, amines, sulphides and epoxidation of alkenes. We have also established a likely mechanistic pathway for these reactions which revealed that, when $\text{PhI}(\text{OAc})_2$ is employed as the terminal oxidant, a $\text{Mn}^{\text{V}}=\text{O}$ species is eventually generated. The same species are also generated when PhIO is employed but a more straight experimental procedure can be achieved by the use of $\text{PhI}(\text{OAc})_2$ as terminal oxidant. It has been established that chloro substituted Schiff base Mn(III) complex has the highest catalytic activity among the three mononuclear Mn(III) complexes of chloro, bromo and iodo

substituted Schiff base ligands. This efficiency is related to steric repulsions established between $\text{PhI}(\text{OAc})_2$ and the metal complexes used in this work as it has been well rationalized by theoretical calculations. Eventually we have devised an economically feasible and energetically efficient catalytic method using the chloro substituted Mn (III)-Schiff base complex, which was structurally modified to magnetically separable nanoparticles, for the selective oxidation of various organic substrates at room temperature. In the proposed protocol, we have utilised easily available basic chemicals as the starting materials, an inexpensive metal catalyst, aerobic reaction conditions, and found tolerance to a wide range of functional groups with operational simplicity. Our future endeavours will focus on designing magnetically separable nanocatalysts with a better catalytic activity and superior loading capacity of catalytically active species and also on broadening the substrate scope.

Supporting Information Summary

Supporting information contains experimental section, FT-IR spectra of complexes **1-3** (S1-S3), UV-vis spectra of complexes **1-3** (S4), ESI-MASS of complexes **1-3** (S5-S7), UV-Vis spectrum of complex **1** in presence of PhIO (S8), FT-IR, PXRD, Solid State UV Spectrum, Thermo gravimetric Analysis of $\text{Fe}_3\text{O}_4@\text{dopa}@\text{MnL}^1\text{Cl}$ (**FDM-1**) (S9-S12), SEM image of reused **FDM-1** (S13), Recyclability and reusability test of **FDM-1** for the oxidation of various substrates (S14), $^1\text{H-NMR}$ of oxidation products (S15-S18) and calculations related to the values of Table 1. Also information regarding coordination bond lengths and angles for both Complex **1** and **2** as obtained from X-Ray determination are provided (Table S1-S2). Different types of interactions in complexes **1** and **2** are shown in Tables S3-S6. CCDC 1498889 and 1498888 contains the supplementary crystallographic data for complexes **1** and **2** respectively. These data can be obtained free of charge from The Cambridge Crystallographic Data Centre via www.ccdc.cam.ac.uk/data_request/cif. Absolute and relative B3LYP/6-31+G(d,p) electronic and Gibbs energies of the reactants and adducts formed in the reaction between manganese complexes and $\text{PhI}(\text{OAc})_2$ oxidant are shown in Table S7. Cartesian coordinates of all the minima (isolated reactants and adducts) $\text{PhI}(\text{OAc})_2$ are shown in Table S8.

ACKNOWLEDGEMENT

Financial assistance from Science and Engineering Research Board (SERB), New Delhi (Grant No.SB/FT/CS-185/2013) to TC is gratefully acknowledged. TC also expresses thanks

to Dr. Soumen Ghosh, Department of Chemistry, University of Calcutta for various scientific discussion.

KEYWORDS: Mn(III)-Schiff base complex, Magnetic separation, Oxidation, $\text{PhI}(\text{OAc})_2$, Reusability

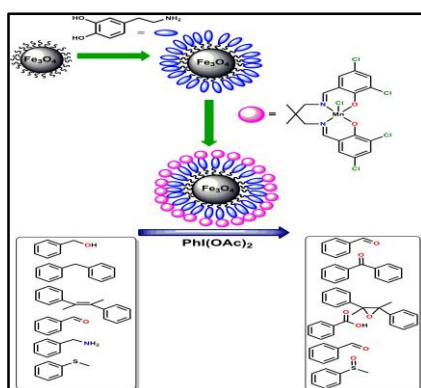
REFERENCES

- [1] M. Hudlucky, *Oxidations in Organic Chemistry*, American Chemical Society, Washington, DC, **1990** (ACS Monograph Series).
- [2] T. Chattopadhyay, M. Kogiso, M. Asakawa, T. Shimizu, M. Aoyagi, *Catal. Commun.* **2010**, *12*, 9-13.
- [3] (a) M.C. Lopez, P.Y. Chavant, F. Molton, G. Royal, V. Blandin, *ChemistrySelect.* **2017**, *2*, 443-450. (b) R.L. Neve, M.C. Eidschink, I. A. Guzei, B.M. Peterson, G.M. Vang, R.W. McGaff. *ChemistrySelect.* **2016**, *1*, 5182 – 5186. (c) R.C. Dey, M.M. Islam, M. Halder, A.S. Roy, S.M. Islam. *ChemistrySelect.* **2016**, *1*, 6797 – 6804.
- [4] G.T. Brink, I.W. Arends, R.A Sheldon, *Science.* **2000**, *287*, 1636-1639
- [5] K. Sato, M. Aoki, J. Takagi , R. Noyori, *J. Am. Chem. Soc.*, **1997**, *119*, 12386 - 12387;
- [6] I. E. Marko, M. Tsukazaki, P. R. Giles, S. M. Brown , C. J. Urch, *Angew. Chem.* **1997**, *109*, 2297 - 2299
- [7] M. Zhao, J. Li, E. Mano, Z. Song, D. M. Tschaen, E. J. J. Grabowski , P. J. Reider, *J. Org. Chem.* **1999**, *64*, 2564 – 2566.
- [8] B. Meunier ,*Chem. Rev.* **1992**, *92* ,1411-1456.
- [9] D. B. Dess , J. C. Martin, *J. Am. Chem. Soc.* **1991**, *113*, 7277–7287.
- [10] D. B. Dess , J. C. Martin, *J. Org. Chem.*, **1983**, *48*, 4155–4156.
- [11] S. D. Meyer , S. L. Schreiber, *J. Org. Chem.*, **1994**, *59*, 7549-7552
- [12] M. Frigerio, M. Santagostino, S. Sputore , G. Palmisano, *J. Org. Chem.* **1995**, *60*, 7272-7276.
- [13] H. Tohma, S .Takizawa , T.Maegawa , Y. Kita, *Angew. Chem.*, **2000**, *112*, 1362-1364.
- [14] W. Adam, F. G. Gelalcha, C. R. Saha-Moëller ,V. R. Stegmann, *J. Org. Chem.* **2000**, *65*, 1915-1918.
- [15] A.D. Mico, R. Margarita, L. Parlanti, A. Vescovi, G. Piancatelli. *J. Org. Chem.* **1997**, *62* , 6974-6977.
- [16] F. Montanari, L. Casella (Eds.), *Metalloporphyrins Catalyzed Oxidations*, Kluwer Academic Publishers, Dordrecht, **1994**

- [17] P. J. Stang, V.V. Zhdankin. *Chem. Rev.* **1996**, *96*, 1123.
- [18] H. Saltzman, J.G. Sharefkin. *Org. Synth.*, **1963**, *43*, 60.
- [19] T. Kitamura, Y. Fujiwara. *Org. Prep. Proc. Int.* **1997**, *29*,409-458
- [20] W. Adam , S. Hajra , M. Herderich , C.R. Saha-Möller, *Org. Lett.* **2000** , *2*, 2773-2776.
- [21] J.P. Collman, A.S. Chien, T.A. Eberspacher, J.I. Brauman. *J. Am. Chem. Soc.* **2000**, *122* , 11098.
- [22] J. P. Collman, L. Zeng, R. A. Decreau. *Chem. Commun.*, **2003** , 2974-2975.
- [23] W. Sun, X. Wu, C. Xia, *Helv. Chim.Acta.* **2007** , *90*, 623.
- [24] H. M. Y Nishiyama, *J. Am. Chem. Soc.*,2000, **122**, 11098-11100.
- [25] H. Nishiyama, T. Shimada, H. Itoh, H.Sugiyama, Y. Motoyama, *Chem. Commun.*, **1997**, 1863-1864.
- [26] D. Mansuy, *Coord. Chem. Rev.* **1993** , *125* , 129–142.
- [27] I. Tabushi, K. Morimitsu, *J. Am. Chem. Soc.* **1984**, *106*, 6871-6872
- [28] J.P. Collman, J. I. Brauman, B. Meunier, T. Hayashi, T. Kodadek, S. A. Raybuck, *J. Am. Chem. Soc.***1985** ,*107*, 2000–2005;
- [29] J. T. Groves, R. Neumann, *J. Am. Chem. Soc.*, **1987**,*109*, 5045–5047.
- [30] J. P. Collman, X. Zhang, R. T.Hembre, J. I. Brauman, *J. Am. Chem. Soc.* **1990**,*112*, 5356–5357.
- [31] J. P. Collman, X. M. Zhang, V. J. Lee, E.S. Uffelman, J. I. Brauman, *Science*.**1993**, *261* ,1404–1411.
- [32] M. Mazur, A. Barras, V. Kuncser, A. Galatanu, V. Zaitzev, K.V. Turcheniuk, P. Woisel, J. Lyskawa, W. Laure, A. Siriwardena, R. Boukherrouba, S. Szunerits, *Nanoscale* . **2013**, *5*, 2692-2702.
- [33] S. Singamaneni, V.N. Bliznyuk, C. Binek, E.Y. Tsymbal, *J. Mater. Chem.*, 2011, **21** 16819-16845.
- [34] V. Polshettiwar, B. Baruwati, R. S. Varma, *Green Chem.* **2009**, *11*, 127-131.
- [35] S. Shylesh, V. Schunemann, W. R. Thiel, *Angew. Chem.* **2010**, *122*, 3504-3537.
- [36] M. B. Gawande, A. K. Rathi, I. D. Nogueira, R. S. Varma, P. S. Branco, *Green Chem.* **2013**, *15*, 1895–1899.
- [37] M. B. Gawande, P. S. Branco, R. S. Varma, *Chem. Soc. Rev.* **2013**, *42*, 3371–3393.
- [38] J. Adhikary, A. Datta, S. Dasgupta, A. Chakraborty, M.I. Menéndez, T. Chattopadhyay, *RSC Adv.*, **2015**, *5*, 92634-92647.

- [39] T. Chattopadhyay, A. Chakraborty, S. Dasgupta, A. Dutta, M.I. Menéndez, E. Zangrando, *Appl. Organomet. Chem.* **2017**, *31*, e3663.
- [40] B. N. Figgis, M. A. Hitchman, *Ligand Field Theory and its Applications*. Wiley-VCH, USA, **2000**.
- [41] R. K. Dean, C. I. Fowler, K. Hasan, K. Kerman, P. Kwong, S. Trudel, D. B. Leznoff, H-B Kraatz, L. N. Dawe, C. M. Kozak. *Dalton Trans.* **2012**, *41*, 4806-4816.
- [42] A. W. Addison, T. N. Rao, J. Reedijk, J. Van Rijn, G. C. Verschoor, *J. Chem. Soc., Dalton Trans.* **1984**, *7*, 1349.
- [43] B. C. Gilbert, J. R. Lindsay Smith, A. M. Payeras, J. Oakes, R. Pons i Prats, *J. Mol. Cat. A: Chemical.* **2004**, *219*, 265 – 272.
- [44] H. Guo, R. Qian, Y. Liao, S. Ma, Y. Guo, *J. Am. Chem. Soc.* **2005**, *127*, 13060 – 13064.
- [45] L. S. Santos, C. H. Pavam, W. P. Almeida, F.Coelho, M. N. Eberlin, *Angew. Chem.* **2004**, *116*, 4430 – 4433.
- [46] A. D.Mico, R.Margarita, G.Piancatelli, *Tetrahedron Lett.* **1995**, *36*, 3553-3556. (b) S. Creager, R. W.Murray, *Inorg. Chem.* **1985**, *24*, 3824-3828.
- [47] F. Teixeira, M.D.S. Cordeiro, *Catalysts.* **2017**, *7*, 2-27.
- [48] J.P.Collman, L. Zeng, J.I. Brauman, *Inorg. Chem.* **2004**, *43*, 2672-2679.
- [49] C.Wang , T. Kurahashi, K. Inomata, M.Hada, H.Fujii, *Inorg. Chem.* **2013**, *52*, 9557-9566
- [50] V. S. Zaitsev, D. S. Filimonov, I. A. Presnyakov, R. J. Gambino , B. Chu, *J. Colloid Interface Sci.* **1999**,*212*, 49–57.

Table of Contents



Oxidation of a wide variety of organic functionalities with yields greater than 90% were obtained using a magnetically separable nanocatalyst. Here we emphasized upon the role of PhI(OAc)₂ as an oxidizing agent and hence devised a probable mechanism involving it to show the generation of Mn(V)=O species. Our views are further justified by experimental and theoretical approach